Physics research on the TCV tokamak facility: From conventional to alternative scenarios and beyond

(article starts on next page)

PAPER • OPEN ACCESS

Physics research on the TCV tokamak facility: from conventional to alternative scenarios and beyond

View the article online for updates and enhancements.

Recent citations

Physics research on the TCV tokamak facility: from conventional to alternative scenarios and beyond

S. Coda[1], M. Agostini[2], R. Albanese[3], S. Alberti[1], E. Alessi[4], S. Allan[5], J. Allcock[5], R. Ambrosino[6], H. Anand[7], Y. Andrèbe[1], H. Arnichand[1], F. Auriemma[2], J.M. Ayllon-Guerola[8,9], F. Bagnato[1], J. Ball[1], M. Baquero-Ruiz[1], A.A. Beletskii[10], M. Bernert[11], W. Bin[4], P. Blanchard[1], T.C. Blanken[12], J.A. Boedo[13], O. Bogar[14], T. Bolzonella[2], F. Bombarda[15], N. Bonanomi[16], F. Bouquey[17], C. Bowman[18], D. Brida[11], J. Bucalossi[17], J. Buermans[19], H. Bufferand[17], P. Buratti[15], G. Calabró[20], L. Calacci[21], Y. Camenen[22], D. Carnevale[21], F. Carpanese[1], M. Carr[23], L. Carraro[2], A. Casolari[14], F. Causa[4], J. Čeřovský[14], O. Chellaï[1], P. Chmielewski[24], D. Choi[1], N. Christen[25], G. Ciraolo[17], L. Cordaro[2], S. Costea[26], N. Cruz[27], A. Czarnecka[24], A. Dal Molin[16], P. David[11], J. Decker[1], H. De Oliveira[1], D. Douai[17], M.B. Dreval[10], B. Dudson[18], M. Dunne[11], B.P. Duval[1], T. Eich[11], S. Elmore[23], O. Embréus[28], B. Esposito[15], M. Faitsch[11], M. Farník[14], A. Fasoli[1], N. Fedorczak[17], F. Felici[1], S. Feng[16], X. Feng[5], G. Ferró[21], O. Février[1], O. Ficker[14], A. Fil[18], M. Fontana[1], L. Frassinetti[29], I. Furno[1], D.S. Gahle[30], D. Galassi[1], K. Gałązka[24], A. Gallo[17], C. Galperti[1], S. Garavaglia[4], J. Garcia[17], M. Garcia-Muñoz[8,31], A.J. Garrido[32], I. Garrido[32], J. Gath[33], B. Geiger[34], G. Giruzzi[17], M. Gobbin[2], T.P. Goodman[1], G. Gorini[16], M. Gospodarczyk[21], G. Granucci[4], J.P. Graves[1], M. Gruca[24], T. Gyergyek[35], A. Hakola[36], T. Happel[11], G.F. Harrer[37], J. Harrison[23], E. Havlíčková[23], J. Hawke[1], S. Henderson[23], P. Hennequin[38], L. Hesslow[28], D. Hogeweij[39], J.-Ph. Hogge[1], C. Hopf[11], M. Hoppe[28], J. Horáček[14], Z. Huang[34], A. Hubbard[40], A. Iantchenko[1], V. Igochine[11], P. Innocente[2], C. Ionita Schrittwieser[26], H. Isliker[41], R. Jacquier[1], A. Jardin[42], A. Kappatou[11], A. Karpushov[1], P.-V. Kazantzidis[43], D. Keeling[23], N. Kirneva[44,45], M. Komm[14], M. Kong[1], J. Kovacic[35], N. Krawczyk[24], O. Kudlacek[11], T. Kurki-Suonio[46], R. Kwiatkowski[47], B. Labit[1], E. Lazzaro[4], B. Linehan[40], B. Lipschultz[18], X. Llobet[1], R. Lombroni[20], V.P. Loschiavo[3], T. Lunt[11], E. Macusova[14], J. Madsen[33], E. Maljaars[12], P. Mantica[4], M. Maraschek[11], C. Marchetto[4], A. Marco[48], A. Mariani[4], C. Marini[49], Y. Martin[1], F. Matos[11], R. Maurizio[1], B. Mavkov[50], D. Mazon[17], P. McCarthy[51], R. McDermott[11], V. Menkovski[12], A. Merle[1], H. Meyer[23], D. Micheletti[4], F. Militello[23], K. Mitosinkova[14], J. Mlynář[14], V. Moiseenko[10], P.A. Molina Cabrera[1], J. Morales[17], J.-M. Moret[1], A. Moro[4], R.T. Mumgaard[40], V. Naulin[33], R.D. Nem[33], F. Nespoli[22], A.H. Nielsen[33], S.K. Nielsen[33], M. Nocente[16], S. Nowak[4], N. Offeddu[1], F.P. Orsitto[3], R. Paccagnella[2], A. Palha[12], G. Papp[11], A. Pau[52], R.O. Pavlichenko[10], A. Perek[39], V. Pericoli Ridolfini[24], F. Pesamosca[1],

V. Piergotti[15], L. Pigatto[2], P. Piovesan[2], C. Piron[2], V. Plyusnin[27], E. Poli[11],
L. Porte[1], G. Pucella[15], M.E. Puiatti[2], T. Pütterich[11], M. Rabinski[47], J. Juul
Rasmussen[33], T. Ravensbergen[12,39], M. Reich[11], H. Reimerdes[1],
F. Reimold[53], C. Reux[17], D. Ricci[4], P. Ricci[1], N. Rispoli[4], J. Rosato[22],
S. Saarelma[23], M. Salewski[33], A. Salmi[36], O. Sauter[1], M. Scheffer[12],
Ch. Schlatter[1], B.S. Schneider[26], R. Schrittwieser[26], S. Sharapov[23],
R.R. Sheeba[22], U. Sheikh[1], R. Shousha[12], M. Silva[1], J. Sinha[7], C. Sozzi[4],
M. Spolaore[2], L. Stipani[1], P. Strand[28], T. Tala[36], A.S. Tema Biwole[1],
A.A. Teplukhina[54], D. Testa[1], C. Theiler[1], A. Thornton[23], G. Tomaž[35],
M. Tomes[14], M.Q. Tran[1], C. Tsironis[43], C.K. Tsui[1,13], J. Urban[14], M. Valisa[2],
M. Vallar[2], D. Van Vugt[12], S. Vartanian[17], O. Vasilovici[26], K. Verhaegh[18],
L. Vermare[38], N. Vianello[2], E. Viezzer[8,31], W.A.J. Vijvers[39], F. Villone[3],
I. Voitsekhovitch[23], N.M.T. Vu[1], N. Walkden[23], T. Wauters[19], M. Weiland[11],
H. Weisen[1], M. Wensing[1], M. Wiesenberger[33], G. Wilkie[28], M. Wischmeier[11],
K. Wu[20], M. Yoshida[55], R. Zagorski[24], P. Zanca[2], J. Zebrowski[47], A. Zisis[56],
M. Zuin[2] and the EUROfusion MST1 Team[a]

[1] Ecole Polytechnique Fédérale de Lausanne (EPFL), Swiss Plasma Center (SPC), 1015 Lausanne,
Switzerland
[2] Consorzio RFX, Corso Stati Uniti 4, 35127 Padova, Italy
[3] University of Napoli 'Federico II', Consorzio CREATE, Via Claudio 21, 80125 Napoli, Italy
[4] IFP-CNR, via R. Cozzi 53, 20125 Milano, Italy
[5] Department of Physics, Durham University, Durham, DH1 3LE, United Kingdom of Great Britain
and Northern Ireland
[6] University of Napoli Parthenope, Consorzio CREATE, Via Claudio 21, 80125 Napoli, Italy
[7] ITER Organization, Route de Vinon-sur-Verdon, CS 90 046, 13067 St.-Paul-lez-Durance Cedex, France
[8] Centro Nacional de Aceleradores (CNA), Universidad de Sevilla, Junta de Andalucia, Consejo Superior
de Investigaciones Cientificas (CSIC), Parque Cientifico y Tecnologico Cartuja, c/Thomas Alva Edison, 7,
41092 Sevilla, Spain
[9] Department of Mechanical Engineering and Manufacturing, University of Seville, Camino de los
Descubrimientos s/n, 41092 Sevilla, Spain
[10] Institute of Plasma Physics, National Science Center, Kharkov Institute of Physics and Technology,
61108 Kharkov, Ukraine
[11] Max-Planck-Institut für Plasmaphysik, 85748 Garching, Germany
[12] Eindhoven University of Technology, PO Box 513, 5600 MB Eindhoven, Netherlands
[13] University of California, San Diego, Energy Research Center, La Jolla, CA 92093,
United States of America
[14] Institute of Plasma Physics AS CR, Za Slovankou 1782/3, 182 00 Praha 8, Czech Republic
[15] Unità Tecnica Fusione, ENEA C. R. Frascati, via E. Fermi 45, 00044 Frascati (Roma), Italy
[16] Department of Physics 'G. Occhialini', University of Milano-Bicocca, Piazza Della Scienza 3,
20126 Milano, Italy
[17] CEA, IRFM, 13108 Saint Paul Lez Durance, France
[18] York Plasma Institute, Department of Physics, University of York, Heslington, York, YO10 5DD,
United Kingdom of Great Britain and Northern Ireland
[19] Laboratory for Plasma Physics, Koninklijke Militaire School—Ecole Royale Militaire,
Renaissancelaan 30 Avenue de la Renaissance, 1000 Brussels, Belgium
[20] Department of Economics, Engineering, Society and Business Organization (DEIm),
University of Tuscia, Largo dell'Università snc, 01100 Viterbo, Italy
[21] University of Rome Tor Vergata, via del Politecnico 1, 00133 Rome, Italy
[22] Aix-Marseille Université, CNRS, PIIM, 13013 Marseille, France
[23] CCFE, Culham Science Centre, Abingdon, Oxon, OX14 3DB, United Kingdom of Great Britain and
Northern Ireland
[24] Institute of Plasma Physics and Laser Microfusion, Hery 23, 01-497 Warsaw, Poland
[25] Rudolf Peierls Centre for Theoretical Physics, University of Oxford, Oxford, Oxon, OX1 3PU, United
Kingdom of Great Britain and Northern Ireland
[26] Institut für Ionen- und Angewandte Physik, Universität Innsbruck, Technikerstraße 25, 6020 Innsbruck,
Austria
[27] Instituto de Plasmas e Fusão Nuclear, Instituto Superior Técnico, Universidade de Lisboa, 1049-001
Lisboa, Portugal

28 Department of Physics, Chalmers University of Technology, 41296 Gothenburg, Sweden

29 Fusion Plasma Physics, EES, KTH, 10044 Stockholm, Sweden

30 Department of Physics SUPA, University of Strathclyde, Glasgow, G4 0NG, United Kingdom of Great Britain and Northern Ireland

31 Department of Atomic, Molecular and Nuclear Physics, University of Seville, 41012 Sevilla, Spain

32 Faculty of Engineering, University of the Basque Country (UPV/EHU), Paseo Rafael Moreno 3, 48013 Bilbao, Spain

33 Department of Physics, Technical University of Denmark, Bldg 309, 2800 Kgs Lyngby, Denmark

34 Max-Planck-Institut für Plasmaphysik, Teilinstitut Greifswald, 17491 Greifswald, Germany

35 Jožef Stefan Institute, Jamova 39, 1000 Ljubljana, Slovenia

36 VTT Technical Research Centre of Finland Ltd, PO Box 1000, 02044 VTT, Finland

37 Institute of Applied Physics, T.U. Wien, Fusion@ÖAW, Wiedner Hauptstr. 8-10, 1040 Vienna, Austria

38 Laboratoire de Physique des Plasmas, CNRS UMR7648, Ecole Polytechnique, 91128 Palaiseau, France

39 FOM Institute DIFFER 'Dutch Institute for Fundamental Energy Research', 5600 HH Eindhoven, Netherlands

40 Plasma Science and Fusion Center, Massachusetts Institute of Technology, Cambridge, MA 02139, United States of America

41 Aristotle University of Thessaloniki, 54124 Thessaloniki, Greece

42 Institute of Nuclear Physics Polish Academy of Sciences (IFJ PAN), 31-342 Krakow, Poland

43 National Technical University of Athens, 10682 Athens, Greece

44 Institute of Physics of Tokamaks, National Research Center 'Kurchatov Institute', 123182 Kurchatov Sq., 1, Moscow, Russian Federation

45 National Research Nuclear University MEPhI (Moscow Engineering Physics Institute), 115409, Kashirskoe Sh., 31, Moscow, Russian Federation

46 Department of Applied Physics, Aalto University, 00076 Aalto, Finland

47 National Centre for Nuclear Research (NCBJ), 05-400 Otwock, Poland

48 Advanced Design & Analysis Department, IDOM, 48015 Bilbao, Spain

49 General Atomics, PO Box 85608, San Diego, CA 92186, United States of America

50 Department of Electrical and Electronic Engineering, University of Melbourne, Victoria 3010, Australia

51 Department of Physics, University College Cork, Cork, Ireland

52 Department of Electrical and Electronic Engineering, University of Cagliari, Piazza d'Armi, 09123 Cagliari, Italy

53 Forschungszentrum Jülich GmbH, Institut für Energie- und Klimaforschung—Plasmaphysik, 52425 Jülich, Germany

54 Princeton University, Princeton, NJ 08544, United States of America

55 National Institutes for Quantum and Radiological Science and Technology, Naka, Ibaraki 311-0193, Japan

56 Department of Physics, National and Kapodistrian University of Athens, 15784 Athens, Greece

E-mail: stefano.coda@epfl.ch

CrossMark

Abstract

The research program of the TCV tokamak ranges from conventional to advanced-tokamak scenarios and alternative divertor configurations, to exploratory plasmas driven by theoretical insight, exploiting the device's unique shaping capabilities. Disruption avoidance by real-time locked mode prevention or unlocking with electron-cyclotron resonance heating (ECRH) was thoroughly documented, using magnetic and radiation triggers. Runaway generation with high-Z noble-gas injection and runaway dissipation by subsequent Ne or Ar injection were studied for model validation. The new 1 MW neutral beam injector has expanded the parameter range, now encompassing ELMy H-modes in an ITER-like shape and nearly non-inductive H-mode discharges sustained by electron cyclotron and neutral beam current drive. In the H-mode, the pedestal pressure increases modestly with nitrogen seeding while fueling moves the density pedestal outwards, but the plasma stored energy is largely uncorrelated to either seeding or fueling. High fueling at high triangularity is key to accessing the attractive small edge-localized mode (type-II) regime. Turbulence is reduced in the core at negative triangularity, consistent with increased confinement and in accord with global gyrokinetic simulations. The geodesic acoustic mode, possibly coupled with avalanche events, has

been linked with particle flow to the wall in diverted plasmas. Detachment, scrape-off layer transport, and turbulence were studied in L- and H-modes in both standard and alternative configurations (snowflake, super-X, and beyond). The detachment process is caused by power 'starvation' reducing the ionization source, with volume recombination playing only a minor role. Partial detachment in the H-mode is obtained with impurity seeding and has shown little dependence on flux expansion in standard single-null geometry. In the attached L-mode phase, increasing the outer connection length reduces the in–out heat-flow asymmetry. A doublet plasma, featuring an internal X-point, was achieved successfully, and a transport barrier was observed in the mantle just outside the internal separatrix. In the near future variable-configuration baffles and possibly divertor pumping will be introduced to investigate the effect of divertor closure on exhaust and performance, and 3.5 MW ECRH and 1 MW neutral beam injection heating will be added.

(Some figures may appear in colour only in the online journal)

1. Introduction

The tokamak à configuration variable (TCV) [1] is a mature European fusion facility, with numerous experiments conducted by international teams organized by the EUROfusion consortium through the medium-size tokamak (MST1) Task Force [2], in parallel with a nearly continuous, self-managed domestic campaign. A versatile device with unparalleled shaping capabilities and flexible heating systems (electron-cyclotron resonance heating (ECRH) and neutral beam heating (NBH)), TCV is employed in a multi-faceted research program ranging from conventional topologies and scenarios in support of ITER, to advanced tokamak scenarios and a broad palette of alternative divertor configurations with an eye to DEMO, to exploratory plasmas driven by theoretical speculation and insight. A strong link with academia and education is enforced organically by TCV's nature as a university facility. As such, generous machine time is provided for training students, who in return provide an essential service as full members of the experimental and operating team. This environment is also naturally conducive to close and productive links with the SPC theory group, which has a strong tradition of analytical and numerical first-principles enquiry, while also managing a panoply of higher-level, interpretation-oriented codes.

The main operating parameters of TCV are as follows: major radius $R = 0.88$ m, minor radius $a = 0.25$ m, vacuum toroidal field $B_T = 1.5$ T, plasma current up to $I_p = 1$ MA. The polarities of both field and current can be chosen at will in any discharge. The primary wall-facing material is graphite. Three piezoelectric valves are used for injection of both the primary discharge fuel and seed impurities; an additional, fast, solenoid-based multi-valve system is available for disruption mitigation through massive gas injection (MGI) (recently upgraded from a previous version for greatly increased gas flow). The defining shaping versatility of the device is provided by a system of 16 independently-powered shaping poloidal-field (PF) coils, in addition to two coils internal to the vessel for control of axisymmetric instabilities with growth rates up to $5000 \, \text{s}^{-1}$.

During most of the device's lifetime, its primary auxiliary heating source has been ECRH, in a combination of second- (X2, 82.7 GHz) and third-harmonic (X3, 118 GHz) X-mode components with a maximum aggregate power of 4.1 MW, injected through up to seven independent launchers [3]. The finite life expectancy of the gyrotron sources has led to a gradual reduction of this power to a current total of 1.15 MW. We are currently in the process of procuring four additional gyrotrons, two 0.75 MW units for X2 waves and two 1 MW dual-frequency units for either X2 or X3 [4]. By the end of 2019 we thus expect to have 3.3 MW X2 and 3.1 MW X3 available at the tokamak end (with a maximum simultaneous total power of 4.5 MW), restoring the plant's erstwhile flexibility in both localized and diffuse heating at virtually all plasma locations in virtually all configurations, with a varying mix of heating and current drive.

Since 2015, NBH has also been employed on TCV, using a 15–25 keV beam of maximum 1 MW power (at the highest energy), in a tangential geometry affording a double pass through the plasma cross-section [5, 6]. A second 1 MW injector, directed in the opposite direction and featuring an energy of 50–60 keV, is currently being planned for the 2020 horizon.

The experimental campaigns are assisted by a continuous program of diagnostic upgrades and development. The Thomson scattering diagnostic was upgraded with the addition of 40 new spectrometers and a redesign of the optical layout to guarantee a more complete coverage of the plasma in all configurations, without spatial gaps and with increased energy resolution particularly for edge measurements [7]. A three-radiator Cherenkov detector was deployed in support of runaway-electron experiments in a collaboration with the National Centre for Nuclear Research in Poland [8]. Runaway studies were also assisted by a runaway electron imaging and spectrometry system detecting infrared and visible synchrotron radiation, on loan from ENEA (Italy) [9]. Tangential, multi-spectral, visible-light camera arrangements have been installed on TCV by groups from MIT (USA) [10] and Eindhoven University of Technology (The Netherlands) [11]. TCV was also equipped recently with a Doppler backscattering

apparatus and a highly novel short-pulse time-of-flight reflectometer, used alternately as they share most of the hardware, including a steerable quasi-optical antenna [12, 13].

This paper reports on scientific results from the past two-year period, during which TCV was operated regularly without major interruptions. Several of the experiments described in this paper also had counterparts in the other operating MST facility, ASDEX Upgrade (AUG) [14]. Section 2 discusses work on abnormal discharge termination events, including disruptions and runaway-electron beam formation; section 3 reports on discharge scenario development and associated real-time control; section 4 deals with core physics, particularly the related issues of transport and turbulence for both the thermal and non-thermal populations; section 5 is on edge and exhaust physics and detachment, both in conventional and alternative-divertor scenarios; the first successful generation of a doublet configuration is discussed in section 6; conclusions and an outlook, including the description of a significant upcoming divertor upgrade, are provided in section 7.

2. Disruption physics

This area had not received sustained attention in the past on TCV and its recent rise to prominence is a particularly good demonstration of successful international collaborations, particularly as catalyzed by the EUROfusion framework.

2.1. Disruptions

Issues related to unwanted discharge termination, being at the forefront of reactor designers' concerns [15], are addressed vigorously in the TCV program. A path-oriented approach [16] has been advanced to deal with the changed perspective of the reactor scale, which remains grounded in safety but has to be mindful of economics. While device integrity remains paramount, value is attached to keeping peak performance as well. This yields a prioritized hierarchy of full performance recovery, disruption avoidance, and disruption mitigation—all of which are dependent upon the specific disruption path [16]. Experiments were performed in parallel on AUG and TCV. On TCV the focus was on disruptions caused by abnormal impurity inflow precipitating a disruptive event caused by the locking of a pre-existing $n = 1$ neoclassical tearing mode (NTM) on the $q = 2$ surface. The impurity inflow was simulated by a massive, controlled injection of a noble gas such as neon. The event detector was a sharp increase in radiation, specifically soft x-ray emission. The application of ECCD on the $q = 2$ surface can prevent the locking altogether or, if applied with some delay, unlock and stabilize the mode, still preventing the disruption. Both full performance recovery and soft landing paths were explored and documented [17]. Higher power and better precision are required to unlock the mode than to prevent locking (figure 1). Prevention was enabled by real-time triggers based on maximum entropy and maximum likelihood techniques applied to magnetic signals [18], or on radiation thresholds. Safe discharge termination through controlled current ramp-down (to 50 kA) was also tested successfully. All

these techniques were finally combined in a first prototype closed-loop feedback system including tracking of the $q = 2$ surface through real-time equilibrium reconstruction [17] and ECRH ray tracing [19].

A path-oriented approach is bound to be costly as the paths to disruption form a large and heterogeneous set, but the techniques developed for the specific path described above have some degree of generic applicability and hold promise for generalization. A version of the strategy described above is under development in the general architecture of supervisory real-time control, including event monitoring through plasma-position and rotating- and locked-mode detection [20], and incorporating actuator management tools [21]. In parallel, an algorithm to detect proximity to the density limit based on changes in sawtooth characteristics was also developed successfully.

An offline disruption database was also constructed using the DIS_tool package, for statistical analysis of disruption triggers and as a basis for prediction and modelling (to be performed using a machine-learning technique already applied successfully to JET [22]). By processing multiple diagnostics, DIS_tool is able to detect fast transient events characterizing the disruptive process, such as thermal quenches and current spikes, and to automatically compute characteristic times and parameters of interest. The parametrization of the algorithm renders it independent of the characteristics of the individual device [23, 24].

2.2. Runaway electrons

Another facet of the discharge termination problem is the production of runaway electrons (RE), which is also a central concern of reactor operation. In ITER, RE beams of up to 12 MA can be expected, with the potential to cause deep damage to the metallic structures. Mitigation and control of RE beams are thus a must. Runaway generation both in steady state and disruptive conditions, at low density and with the aid of high-Z noble gas injection, has been documented in TCV. RE beams are generated on TCV for a broad range of edge safety factor, down to 2.1, and at elongations up to 1.5. Key data on runaway dissipation by subsequent Ne and Ar injection are being used for validation of a high-Z interaction model. The increased throughput of the new MGI valve system has allowed us to quantify the increase in RE dissipation rate with gas injection rate and its dependence on gas species, Ar being more effective than Ne. Initial studies of the effect of ECRH on the RE beam have also been performed. Secondary RE avalanching was identified and quantified for the first time after massive Ne injection; simulations of the primary RE generation and secondary avalanching dynamics in stationary discharges indicate that the RE current fraction created via avalanching could reach 70%–75% of the total plasma current. Relaxation events consistent with RE losses caused by the excitation of kinetic instabilities are also observed [25].

An extensive set of experiments were performed to study the options for controlled ramp-down in the presence of a disruptive event featuring a RE beam. Upon detection of the
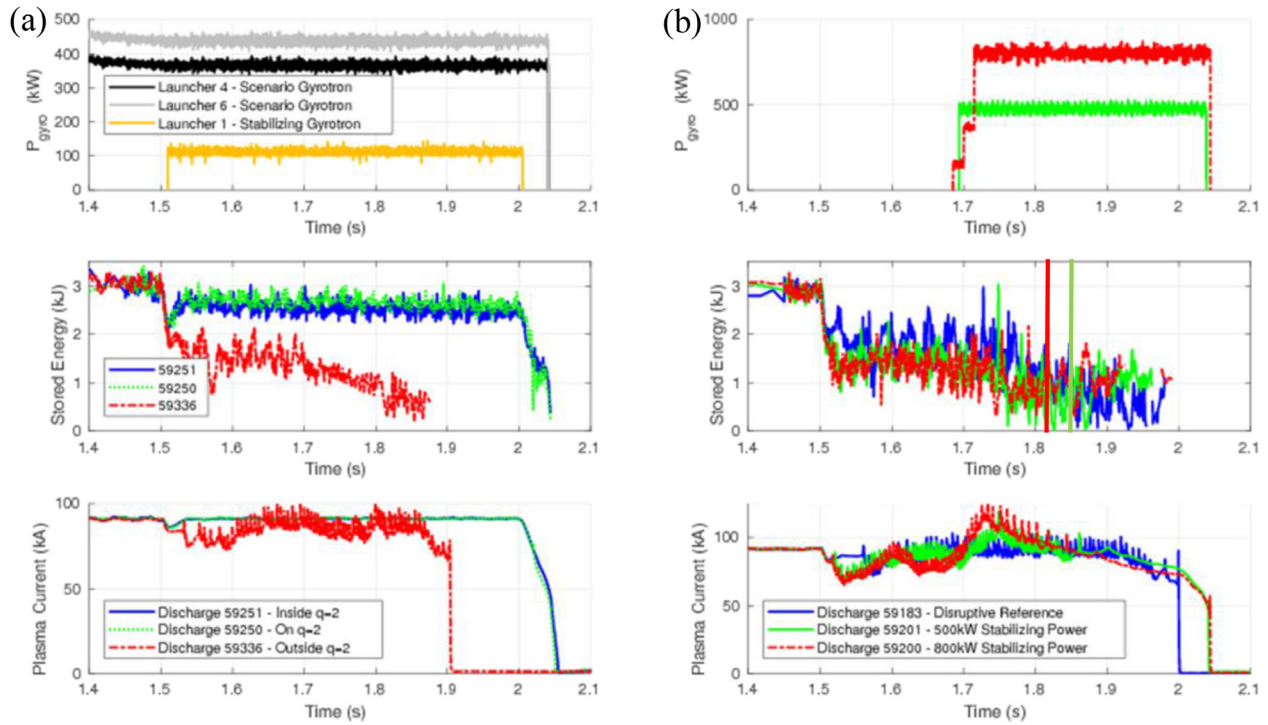
Figure 1. (*a*) Disruption prevention versus (*b*) disruption avoidance: ECRH power (top), stored energy (middle), plasma current (bottom). The disruption prevention plots collect three discharges with identical deposition location for the sources used to destabilize the mode ('scenario gyrotrons') and varying deposition location for the electron cyclotron current drive (ECCD) source used for stabilization, showing that ECCD is effective at stabilizing when it is applied on or just inside the $q = 2$ surface. In this case, one 100 kW ECCD source is sufficient to restore discharge performance when mode locking is prevented. The right-hand plots show that, once the discharge enters the disruptive chain, 500 kW for 150 ms or 800 kW for 110 ms is required for recovery (only the power used for stabilization is plotted here): the times of mode unlocking are indicated by vertical lines in the middle plot. Note that these discharges do disrupt eventually during a controlled rampdown. By contrast, the disruptive reference with no stabilizing action shown for comparison (in blue) disrupts during the flat top as a result of the locked mode. Reproduced courtesy of IAEA. Figure [17]. Copyright (2018) IAEA.

current quench and plateau onset (via current and hard x-ray observers), a dedicated controller takes over. The 'hybrid fast controller', initially developed for the Frascati tokamak upgrade, is empirical, lightweight, easily tunable, and portable [26]. The current ramp-down is controlled through the Ohmic transformer, with assistance from MGI to limit the RE beam's energy, and the beam position is controlled through the PF coils. The ramp-down rate is kept below a threshold to avoid the appearance of deleterious magnetohydrodynamic (MHD) instabilities that can engender a total loss of control. This control scenario appears robust and reproducible (figure 2), and intriguingly, a total conversion of RE current into thermal plasma current has also been observed. This is speculatively attributed to loop-voltage oscillations coupled with system hysteresis, and hints at a possible new termination scenario [26].

3. Scenario development

3.1. Main reactor scenarios

In the most recent campaign a stable ELMy H-mode was obtained in an ITER-like shape permitting direct scaling comparisons with the corresponding AUG scenario [27]. Work in this area has been hampered by the empirical and unexplained

elusiveness of regular edge-localized modes (ELMs) in configurations centered near the vessel midplane, where NBH is located. Of different plasma shapes attempted, the most resilient has proven to be one with low upper triangularity (δ) and high lower δ, which has been taken to $q_{95} = 3.6$ at an elongation of 1.8, with NBH alone as well as NBH+X3. The application of a more ELM-resilient vertical observer in the future could alleviate some of the difficulties with these scenarios and allow also for stable operation at $q_{95} = 3$.

The I-mode [28] has also been pursued, primarily mimicking the equivalent low-δ shape of AUG. NBH not being sufficient to reach I- or H-mode in this configuration, X3 was added, unsuccessfully at $B_T = 1.35$ T but with some promising recent developments at $B_T = 1.53$ T.

The goal of the Advanced Tokamak route was to extend to higher β_N, using NBH and X3, well-known fully non-inductive scenarios with internal transport barriers (ITBs) and high bootstrap current fraction achieved in the past in TCV with X2 ECCD. It has not proven possible thus far to obtain non-inductive ITBs with NBH, its diffuse or central heating and modest current drive contribution being detrimental to the establishment of negative magnetic shear in the center. Conversely, ITBs with ECCD and NBH were studied for the first time, but could not be sustained non-inductively [29]. Non-inductive discharges in L-mode were sustained at
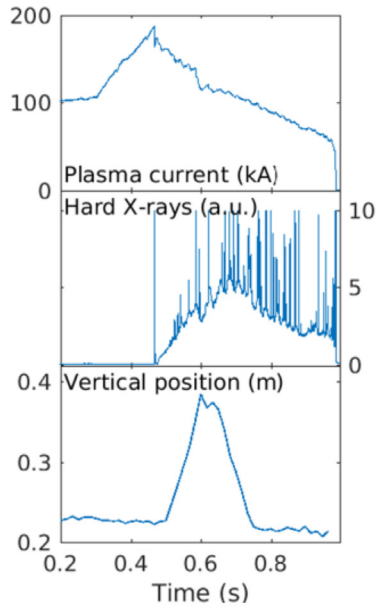
Figure 2. Demonstration of RE ramp-down with the hybrid fast controller with vertical 11 cm sweep. Plasma current (top), hard x-ray emission (middle), vertical position of magnetic axis (bottom). Reproduced from [26]. © IOP Publishing Ltd. All rights reserved.

$I_p = 130$ kA, H-factor $H_{98(y,2)} = 0.8$, and $\beta_N = 1.4$. A successful attempt at H-mode was made in nearly non-inductive conditions, by targeting a low enough density in H-mode to be compatible with X2 heating. The result is shown in figure 3, with $H_{98(y,2)} = 1$ and $\beta_N = 1.7$ [30]. The neutral-beam deposition and fast-ion dynamics are being modeled with the NUBEAM-ASCOT code suite for these scenarios [31]. The additional power expected for the next campaign holds promise for improving performance.

Finally, TCV has long established the merits of negative triangularity, which is now being considered as a serious candidate for a test reactor. All this work was performed in limited shapes and, more recently, in diverted shapes with negative *upper* triangularity. Finally, stable, negative-triangularity single-null-diverted shapes, fully mirroring conventional diverted discharges, were developed for the first time in the last campaign but have not yet been successfully established in a NBH-compatible location.

3.2. Real-time control

Many achievements in the past campaign were either made possible or at least aided by advancements in plasma control. In this subsection progress on different specific aspects of control will be presented briefly in turn, concluding with the work performed on integration and unification.

In the area of MHD control, work on NTMs continues to feature prominently, with increasing refinements in characterization and understanding. It has been determined that NTM destabilization through central co-ECCD only occurs within a given density range [32]. For the first time, the application of a periodic (sinusoidal) deposition-location sweep has been
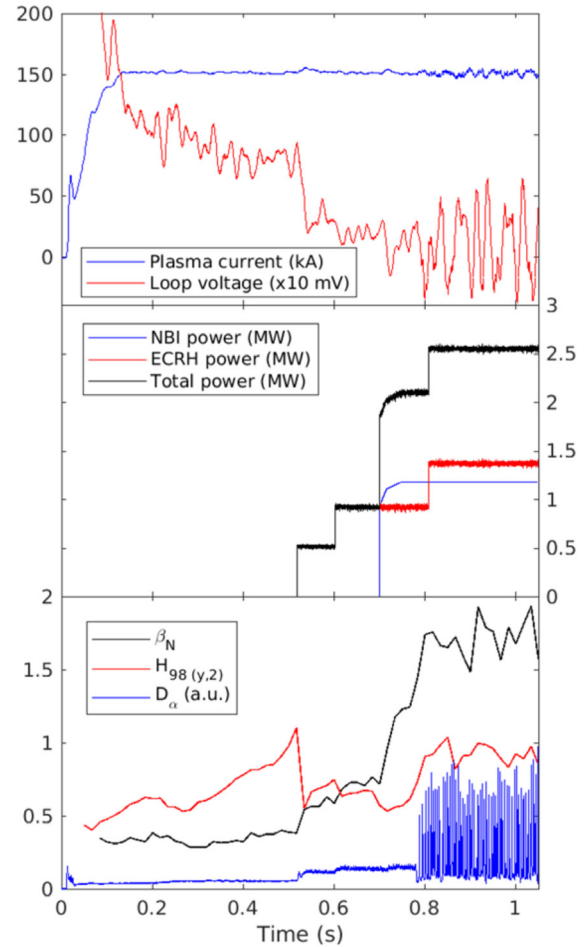
Figure 3. Nearly fully non-inductive H-mode discharge: (top) plasma current and loop voltage; (middle) auxiliary power; (bottom) β_N, $H_{98(y,2)}$, D_α emission. Reproduced with permission from [30].

shown to be effective for both pre-emption and stabilization of the (2,1) NTM, the latter requiring more than twice as much power as the former. A simple new analytical model for the time history of the magnetic Δ' stability index, for NTMs triggered as classical tearing modes, was introduced and shown to provide accurate simulations of the island evolution [33]. Quasi-in-line ECE, nearly counter-linear with the associated ECRH actuator, was tested on TCV for monitoring the island's position, and was demonstrated to be accurate to within less than the EC beam width [34]. Though receiving less attention than NTMs in recent times, the vertical axisymmetric instability also remains a concern; while the (magnetic) stabilization technique is well understood, its economics are strongly affected by the minimum achievable stability margin in any given device. In this perspective, experiments were carried out in TCV using elongation ramps to provide data for model validation [35].

In a unique multi-institutional collaborative effort, TCV functioned as a testbed for an eclectic ensemble of current-profile control strategies, within a unified framework using the tokamak profile simulator RAPTOR for offline testing. Various highly specialized controllers (model-predictive [36], Lyapunov-based [37], and interconnection and damping assignment-passivity based control [38]) were all tested and

validated successfully using this paradigm. A parallel activity has seen the development of alternative, exploratory current control methods—based on so-called sliding mode and super-twisting controllers—specifically for TCV, yet to be tested [39]. In a related development, a model-based detector of L–H and H–L transitions and of ELMs was used successfully to actuate a power reduction and consequently a back-transition to L-mode, thus avoiding the disruptions that typically terminate ELM-free H-modes.

A shape and position controller, using boundary flux errors and based on a singular-value decomposition approach, was delivered in a complete time-varying version and applied in particular to advanced divertor configurations such as snowflakes [40]. One limitation of this control scheme is its inherent coupling with vertical stability control, making its optimization highly dependent on the particular configuration. To obviate this problem, a new, decoupled set of controllers is currently under development, with promising initial tests already performed on TCV [41].

The RAPTOR code, updated with new time-varying terms [42], was employed in a general effort towards the optimization of the ramp-down phase of tokamak discharges, using appropriate transport models including the L–H and H–L transition dynamics. The optimization is found to include in particular an early H–L transition and a sharp elongation reduction to reduce the internal inductance. Promising initial tests were performed on TCV, pointing the way to possible automation of the optimization procedure [43].

Real-time equilibrium reconstruction, now routinely available on TCV with sub-ms resolution (RTLIUQE), is at the crux of modern tokamak control. From this consideration stems the need to improve over simple magnetic reconstruction, by using kinetic constraints available in real time: a kinetic equilibrium reconstruction suite compatible with real-time needs has accordingly been developed for TCV [44]. In parallel, efforts towards a unified European reconstruction code have turned an eye to TCV as a particularly challenging reconstruction problem, and first reconstructions with the EQUAL/EQUINOX codes have been obtained and benchmarked with RTLIUQE [45].

Controller integration is steadily progressing: NTM, β_N, safety factor (estimated by RAPTOR), density, and shape were shown to be controlled simultaneously. Key to this is the constant development and addition of new elements as need dictates: NBH power control and readback, ECRH power and launcher readback were recently incorporated in the digital control system; the TORBEAM (real-time ECRH beam-tracing) [46] module was also added and RABBIT (NBH deposition) [47] is currently being integrated. A shift from controller-based to task-based control is underway. The architecture for task-based integrated control separates state estimation and event detection from decisions related to actuators. A supervisory controller coordinates the execution of multiple control tasks by assigning priorities based on the plasma state and on the discharge [21]. Crucially, this entire layer is tokamak-agnostic by construction, providing a level of abstraction to discharge planning [48]. The tokamak-specific interfaces are also standardized to minimize exceptions. New

controllers may be tested and integrated continuously using a unified controller test environment comprising RAPTOR and several common algorithms.

3.3. Wall cleaning and start-up assist with ECRH in support of JT-60SA operation

TCV has been used to test techniques anticipated for the successful operation of JT-60SA [49], which will also feature a carbon wall. Characterization of wall cleaning with ECRH, as a substitute for glow discharge cleaning (GDC), has continued from the previous campaign [50]. Additionally, experiments were performed on ECRH-assisted start-up at reduced loop voltage (electric field 0.7 V m^{-1}, consistent with JT-60SA) with residual gas and/or impurities, such as would be expected after a disruption or generally with a shortened shot cycle. The question addressed by this work is of equal importance for DEMO. The minimum ECRH power required for breakdown and successful burn-through was determined by controlling the power from a plasma-current observer. Experimental tests included variations in deuterium prefill, reductions in inter-shot pumping speed (down to 25%), and puffing of Ar impurities, always without the GDC customarily performed between TCV discharges. It was found that 0.4 MW ECRH at the reduced 0.7 V m^{-1} electric field was sufficient to start the plasma and sustain the plasma current, except with Ar injection, which increased the threshold. The results of this experiment are used to validate the 0D breakdown code BKDO, which is coupled with the beam tracing code GRAY to model the ECRH propagation [51].

4. Pedestal and core physics

4.1. Transport and confinement

The physics mechanisms underlying the different scenarios are explored through systematic parametric studies making use of all available diagnostics. The H-mode pedestal is under particular scrutiny, as it can play a formidable role in determining the global confinement in conditions of stiff core profiles. As both fueling and impurity seeding will likely be necessary in a reactor, the latter for heat load control, it is especially important to determine their effect on the pedestal and on confinement. Such a systematic study was performed on TCV in the latest campaign, in a type-I ELMy H-mode, with the addition of a shaping variable, i.e. triangularity. Specifically, a deuterium gas fueling scan and two nitrogen puffing scans—one with no fueling and one with constant fueling—were performed at two different values of the triangularity [52]. It is found that D2 fueling increases the density pedestal height and moves it outwards; interestingly, the shift is in the opposite direction to AUG [53], a metal-wall machine where it is speculated that the high-field-side high-density front observed there could play a role. The pressure pedestal height displays a generally decreasing trend with increased gas injection (figure 4). The sensitivity to fueling and seeding increases with triangularity. However, the total stored energy is largely unaffected by these changes, indicating that the core profiles do
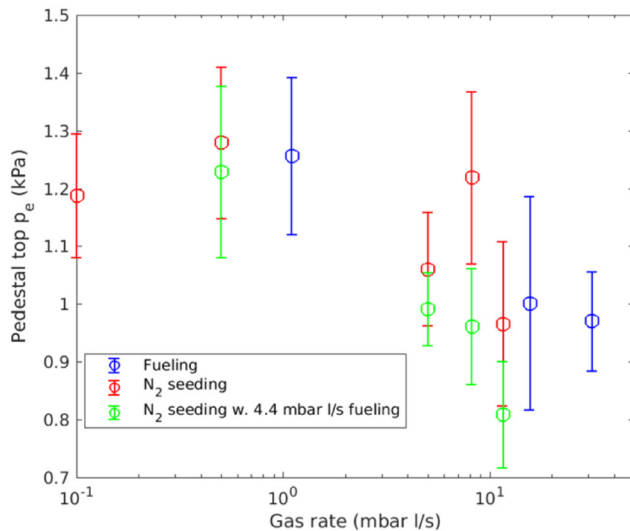
Figure 4. Pressure at the top of the pressure pedestal as a function of fueling or impurity seeding gas injection rate for the low-triangularity case. Reproduced from [52]. © IOP Publishing Ltd.

not remain strictly stiff during these scans—or more accurately, they are not stiff with respect to varying fueling and seeding. An MHD stability analysis indicates that these scenarios are close to the ideal stability limit, where the pedestal is defined by the peeling–ballooning (PB) limit: in the widely-used EPED1 model [54], the evolution of the pedestal leads it to reach the kinetic-ballooning-mode (KBM) limit first, which sets the marginally stable pressure gradient, and then to continue increasing in both width and height until the PB limit is attained, which precipitates an ELM crash. This model yields a pedestal width scaling which makes it proportional to the square-root of the poloidal β at the pedestal top—the proportionality factor being generally machine-dependent. The current dataset is in fact not fitted by this relation with a single constant, but EPED1 modeling gives satisfactory results when the experimentally derived factor is used, confirming that the scenarios are likely to be PB-limited [52].

In spite of apparent differences in the phenomenology, a unified picture is in fact found among TCV, AUG, and JET-ILW in the PB-limited pedestal regime. While the underlying cause of the pedestal shift and particularly of its direction is not understood, the pedestal evolution in response to this shift is consistent: an outward shift of the pressure pedestal reduces its stability and lowers the pedestal height [55].

The properties of the pedestal in earlier discharges with negative upper triangularity [56] were also revisited to evaluate the attractiveness of a negative-triangularity reactor. In these discharges, the shift to negative upper triangularity mitigated the ELMs, increasing their frequency and decreasing the power loss per ELM. The EPED1 model [54] was coupled with a suite of codes commonly used for TCV in the so-called EPED-CH implementation. It was established that negative upper triangularity restricts the KBM + PB-stable domain by closing the second-stability region for ballooning modes, thus further limiting the pedestal's width and height, with the result of mitigating the power expelled by ELMs [57]. Whether this

very attractive feature would come at the expense of reduced core performance remains to be determined, e.g. through transport modelling.

Significant progress has been made in establishing a robust small-ELM regime in TCV. Following the lead of the type-II ELMy regime in AUG [58], grassy ELMs were obtained at high triangularity and steady fueling, replacing the type-I ELMs completely at a triangularity $\delta = 0.54$ (figure 5). The auxiliary heating used in this experiment was 1 MW NBH plus 0.75 MW X3 ECRH. This configuration approaches a double-null shape and the role of the secondary X-point is difficult to disentangle from that of triangularity. The pedestal profiles are remarkably similar in the two discharges shown in figure 5 and the stored energy is thus also similar. However, the peak heat flux in the grassy-ELM regime is reduced by a factor of ten with respect to type-I ELMs, approaching in fact the inter-ELM level of the latter case [59]. In a related development, initial tests were performed for a planned revisitation of ELM pacing through vertical kicks, using new features in the TCV control system [60]. The basic physics of the L–H transition also continues to be explored, with current emphasis on transitions induced by a varying divertor leg length in an otherwise stationary plasma.

Understanding the generation of intrinsic rotation and the mechanisms governing momentum transport is another crucial goal, as rotation is a central ingredient in all scenarios through its inter-relation with transport of energy and particles and with MHD stability. Techniques were developed in the latest campaign to modulate the intrinsic torque in a controlled way for reliable quantitative estimation of intrinsic versus externally-induced rotation. This involves modulation of both the heating and the diagnostic neutral beam, with a complex phasing relationship, and unraveling the data while accounting for the perturbative nature of heating. A thorough documentation of the dependence of intrinsic rotation on density, edge safety factor, and auxiliary power is also underway. Gyrokinetic simulations have suggested a correlation between the toroidal rotation inversion observed when crossing a density threshold with a transition from an ion-temperature-gradient (ITG) dominated to a mixed ITG-trapped-electron-mode (TEM) turbulence regime [61]. Turbulence-driven residual stress is predicted to depend strongly on the up-down asymmetry of the plasma cross-section, which can be parametrized in terms of elongation, triangularity, and tilt angle [62]: these predictions are also being tested in a broad shaping scan. A detailed study of the evolution of rotation during the sawtooth cycle has shown that a co-current torque occurs in the core at the sawtooth crash, in addition to the expected fast outward transport of momentum [63]. Finally, the first characterization of the changes in impurity flow occurring at the L–H transition was obtained on TCV, revealing the familiar formation of a narrow and deep radial-electric-field well just inside the separatrix [63].

The fundamental physics associated with the high-power heating systems is being investigated through the properties, and particularly the confinement, of suprathermal particles. Alfvén modes were recently observed on Mirnov signals for the first time, in the presence of simultaneous off-axis NBH
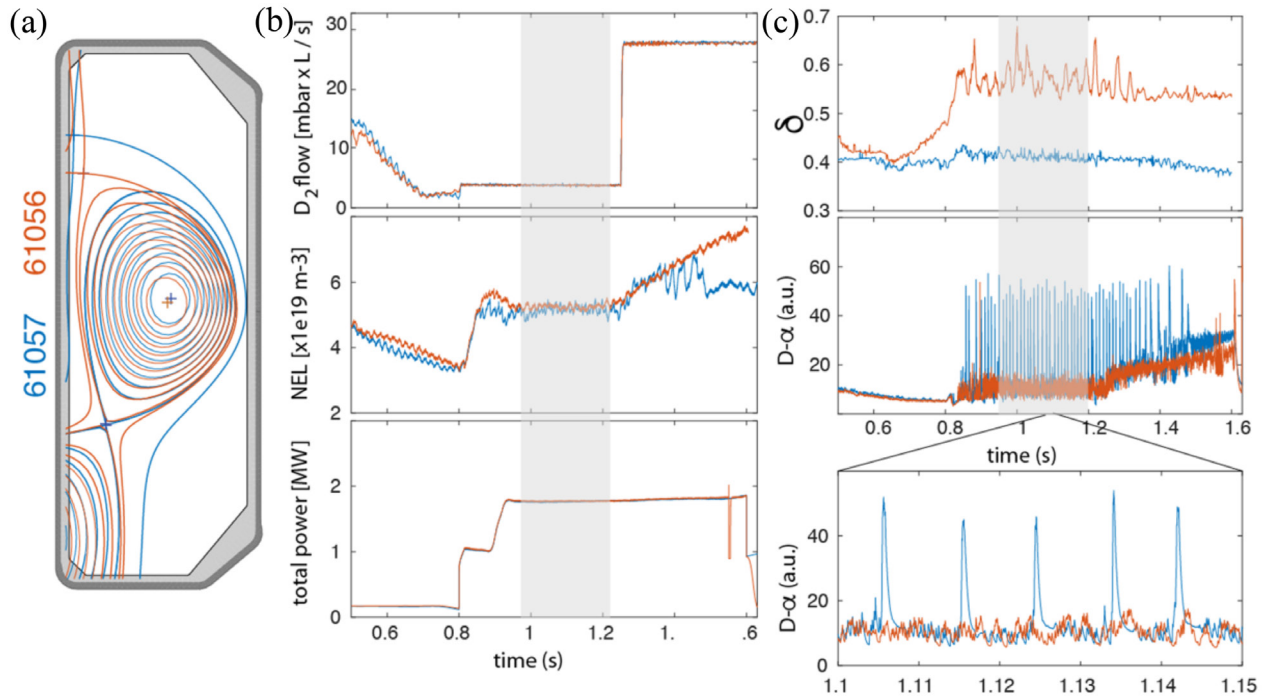
Figure 5. Change in ELM character (from type-I to type-II) related to change in upper triangularity for otherwise similar discharges; key parameters are $q_{95} = 4.5$, elongation $\kappa = 1.5$, ratio of separatrix to pedestal density $= 0.25$, normalized pedestal collisionality $\nu^*_{ped} \sim 2$: (*a*) equilibrium reconstructions; (*b*) from top to bottom: injected gas flow, line-integrated density, total power; (*c*) average edge triangularity and D_α emission, with a zoomed-in detail. Reproduced with permission from [59].

and off-axis ECRH. These modes are only seen with ECRH. Fast-ion measurements by FIDA and NPA diagnostics are used in conjunction with the evolution of the main plasma parameters to model the dynamics of NBH; a high edge neutral density—consistent with charge-exchange losses of the order of 25%—is required to explain the results, but a FIDA signal deficit remains in the case of NBH + ECRH, possibly suggesting enhanced turbulent transport [64].

4.2. Turbulence

A set of fluctuation diagnostics including tangential phase-contrast imaging (tPCI), correlation ECE, and more recently Doppler backscattering and short-pulse reflectometry are employed in fundamental studies of plasma turbulence. The long-standing observation of a clear improvement in confinement in plasmas with negative-triangularity shape compared with positive-triangularity ones [65] has led to an extensive set of studies of the dependence of turbulence on triangularity. Comparisons were made between discharges at $\delta < 0$ and $\delta > 0$, in conditions of equal heating (Ohmic and ECRH) as well as with different heating but matched pressure profiles. In each case a clear suppression in both density and temperature fluctuations is observed with $\delta < 0$, more prominent in the outer region of the plasma but extending deep in the core, approximately to mid-radius (figure 6) [66, 67]. The correlation length and decorrelation time of the broadband fluctuations also decrease with $\delta < 0$. An additional effect of negative triangularity appears to be an increase in the critical gradient for the core pressure profile [66]. As for the variation in anomalous transport, this difference in turbulence
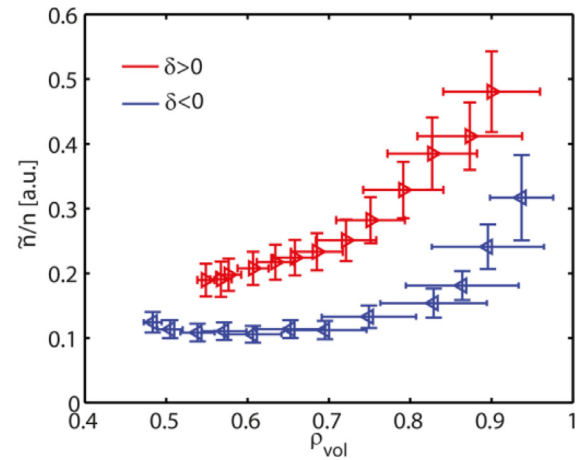
Figure 6. Density fluctuation amplitude profile measured by tPCI in two plasmas with edge triangularity $+0.5$ and -0.3, respectively, with 0.45 MW central ECRH. Reproduced from [67]. © IOP Publishing Ltd. All rights reserved.

characteristics deep in the core suggests the existence of nonlocal effects, since the local triangularity vanishes there. Global gyrokinetic simulations are broadly in accord with the experimental results [68]. In complementary experiments, the fluctuation amplitude was found to decrease with increasing effective collisionality in the TEM-dominated regime [67], consistent with the stabilizing effect of collisionality on these modes and, again, consistent with an attendant improvement in confinement [65].

A mode with the characteristics of the geodesic acoustic mode (GAM), possibly coupled with avalanche events, is

routinely observed on TCV. It sometimes takes the appearance of a continuum mode, with frequency varying with the minor radius according to its linear dependence on the ion sound speed; while in other cases it exhibits a constant frequency over the spatial extent it occupies, typically the outermost third of the plasma cross-section. The physical quantities governing the GAM type are not yet understood, but recent tPCI measurements have shown for the first time a transition from the former to the latter mode in a single discharge, during a safety-factor scan in an ECRH-heated L-mode plasma [69]. Gyrokinetic simulations, however, suggest that the varying density and temperature during the scan, rather than the safety factor itself, may be the cause of the transition [70]. For the first time, this GAM-like oscillation has been detected by scrape-off-layer (SOL) diagnostics near the strike points of diverted plasmas. This includes photodiodes observing D_α emission, wall-embedded Langmuir probes, and magnetic probes. The mode has a high degree of correlation with the core mode measured by tPCI and suggests that it drives a particle flow to the wall. These observations were documented in conventional single-null and double-null shapes as well as alternative divertor configurations such as snowflake (SF) and super-X plasmas [69].

In addition to causing anomalous transport, turbulence can have deleterious effects also on the propagation of externally launched waves; it is feared for instance that strong SOL fluctuations can refract and scatter the mm-wave beams used for ECRH and ECCD and broaden them to the point where the efficacy of, e.g. tearing mode stabilization would be sharply reduced. Dedicated experiments were carried out on TCV to quantify this effect, using a simple setup consisting of the vertically-launching X3 antenna, located at the top of the vessel, coupled with a microwave detector at the bottom [71]. Conditional sampling techniques were used to determine the degree of correlation of oscillations in the transmitted power with fluctuations in the top SOL traversed by the beam. To calculate the beam perturbation, a full-wave code was implemented in COMSOL and benchmarked against the WKBeam code. The Global Braginskii Solver (GBS) code was employed to compute the SOL fluctuations, with input from experimental profiles. This analysis suite was able to demonstrate a causal relationship between the SOL fluctuations and the power transmission oscillations, which exceed 20% in a simple L-mode plasma. In H-mode, similar perturbations are seen to be caused by ELMs (figure 7), although the exact physical mechanism still remains to be clarified [71].

5. Edge and exhaust physics

Exhaust physics remains a central concern of the TCV program, which features the broadest range of divertor topologies, from conventional single- and double-null, to all versions of the snowflake concept, to super-X and beyond. This section reports in turn on results related to divertor detachment, on heat load dynamics in attached conditions, and on SOL transport and fluctuations.
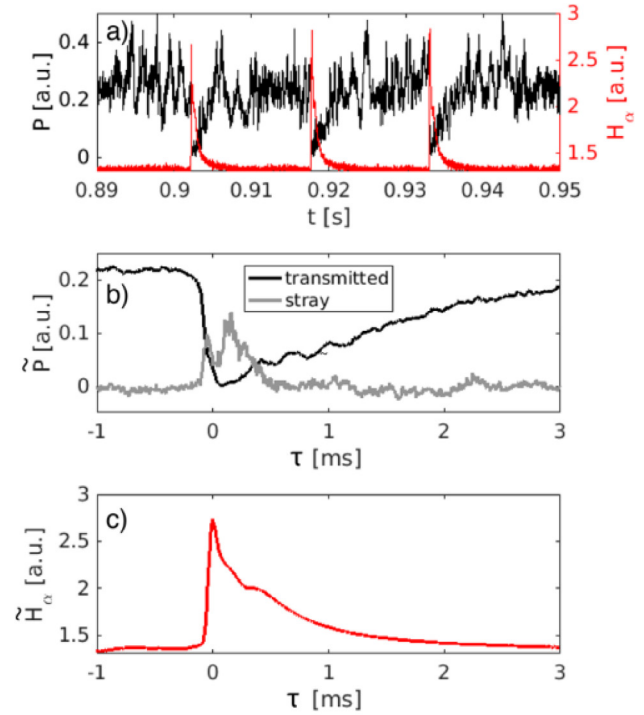
Figure 7. (*a*) Transmitted X3 power versus ELMs detected through D_α emission; (*b*) conditionally-sampled transmitted and stray powers in the ELM cycle (*c*). Reproduced from [71]. © IOP Publishing Ltd. All rights reserved.

5.1. Divertor detachment

5.1.1. L-mode. Detachment is studied primarily through density ramps and impurity seeding. In Ohmic L-mode plasmas, detachment achieved either by fueling or nitrogen seeding results in a reduction of the heat and particle loads at the strike points, as shown by both Langmuir probes (LPs) [72] and infrared thermography [73, 74]. Only the outer target detaches in the case of fueling, whereas both the inner and outer targets detach in the case of seeding. Also, the familiar density 'shoulder' in the upstream SOL profile only appears in the former case [74].

Novel spectroscopic analysis techniques [75] have yielded profiles of divertor ionization and recombination rates and of radiation along the divertor leg, which clearly demonstrate that detachment is caused by power 'starvation', i.e. a reduction in the ionization power source, combined with an increase in the energy required per ionization. Volume recombination plays only a minor role except with deep detachment at the highest densities reached. This is in agreement with analytical predictions as well as SOLPS simulations [76]. Momentum losses of up to 70% develop along with power starvation and the onset of detachment, with charge exchange reactions dominating over ionization.

5.1.2. H-mode. Leveraging on the experience accumulated in L-mode detachment studies in previous campaigns, attention has moved primarily to H-mode in the latest run. Contrary to the L-mode case, the forward-field configuration—with the ion ∇B drift directed towards the X-point—was used to
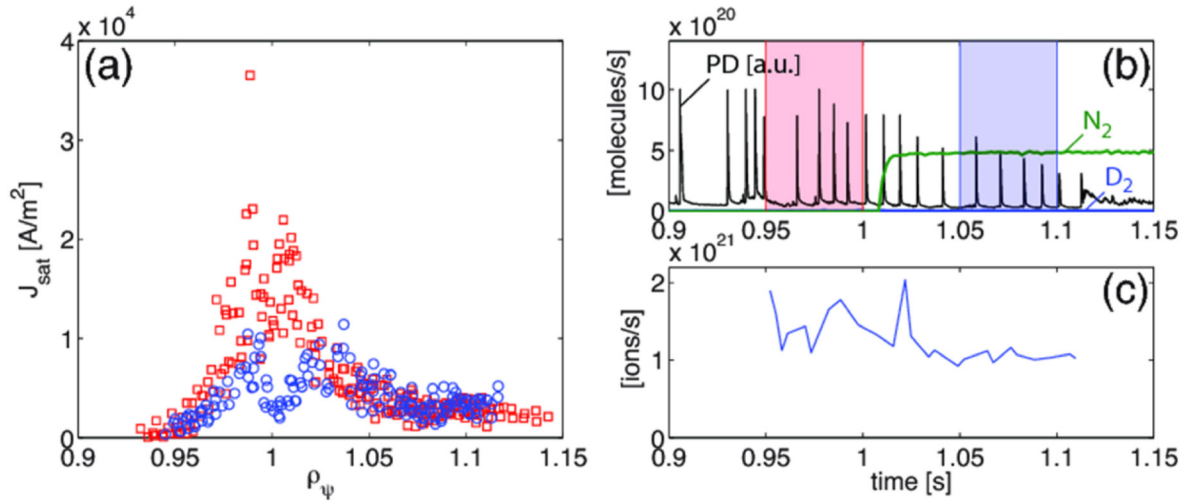
Figure 8. Effect of nitrogen seeding on inter-ELM outer-target saturation-current profiles: (*a*) ion-saturation profiles from LPs in intervals before and after seeding; (*b*) D$_\alpha$ photodiode signal and nitrogen and deuterium injection rates; (*c*) integrated ion flux to outer target. Reproduced with permission from [77].

facilitate the L–H transition. As the parameter space for stable ELMy H-mode accessible by NBH is relatively limited, a multi-pronged approach was pursued [77]. The clearest indications of partial detachment have been obtained at $q_{95} = 3.9$ ($I_p = 210$ kA); scans in divertor geometry, including X- and super-X configurations, were however conducted at $q_{95} = 4.6$ ($I_p = 170$ kA), where the ELMy H-mode regime is more robust; and to extend the study to low q_{95}, detachment dynamics was also studied in ELM-free H-modes, as this is the regime naturally obtained at $q_{95} = 2.4$ ($I_p = 340$ kA). Line-averaged density in the ELMy plasmas is near the minimum in L–H power threshold as a function of density (5×10^{19} m^{-3}). The power threshold itself is found to be largely insensitive to the divertor geometry (including the snowflake-minus, or SF-, case). Detachment was again sought with both fueling and nitrogen seeding. In the ELMy regime, partial inter-ELM detachment of the outer target was observed only with dominant seeding, with attendant power-load mitigation by a factor of two, a 30% reduction in ion saturation current accompanied by a change in its profile (figure 8), and the familiar upstream migration of the N II and C III radiation fronts towards the X-point [77]. Detachment in low-q ELM-free H-modes was also accompanied by a power-load reduction by a factor of two but no measurable decrease in the total particle flux. This regime is inherently non-stationary and short-lived (~200 ms) as the density increases uncontrollably until a disruptive limit is encountered.

Analogously to previous L-mode investigations, scans of flux expansion were performed. The total flux was varied by sweeping the outer leg, varying the major radius of the outer target by 40%. As in L-mode, this has no direct effect on the detachment process, although in the ELMy cases the movement of the impurity emission front (a proxy for divertor cooling) is 20% slower at the largest radius [78]. Simulations with SOLPS are able to reproduce the insensitivity to strike-point radius, attributing it to the competing and counter-varying effects of flux expansion and power losses by ionization

and radiation (stronger at small radius). Scans in poloidal-flux expansion were also performed at fixed target radius. In the ELMy case, detachment shows signs of more H-mode resilience to nitrogen and a stronger drop in particle flux at large flux expansion, and radiation along the outer leg is increased, although the radiation fraction is far lower than in L-mode [77]. ELM-free plasmas, attached or detached, exhibit a drop in particle and heat flux to the outer target with increasing flux expansion. This effect is attributed to a redistribution of the fluxes between the two targets (see section 5.2.1), which could dampen the benefit of flux expansion in a reactor [79].

5.2. Heat-load dynamics

5.2.1. Diverted plasmas. The issue of heat loads on the first wall, of crucial importance for the safe operation of a reactor, is intimately tied to SOL transport physics. The SOL heat-flux profiles, which are measured by infrared thermography, are almost universally parametrized using a main-SOL upstream-remapped power decay length (λ_q) and the so-called *spreading factor* (S), which describes the transport scale length in the divertor SOL [80]. Experiments were performed in attached, SN, Ohmic, low-density plasmas in TCV, in which the connection length was modified without a concomitant change in poloidal flux, by varying the vertical position of the plasma and thus the divertor leg length [81]. It was found that S is unaffected by this change, whereas λ_q increased monotonically with the leg length. A modeling effort with the simple Monte Carlo particle tracer (MONALISA) as well as with the comprehensive transport code SolEdge2D-EIRENE assuming diffusive cross-field transport yields good agreement with the experimental heat flux in the short-leg case. As the leg becomes longer, however, the effect of ballooning turbulence at and below the X-point becomes more important. This is revealed by the first-principle turbulence code TOKAM3X [81], run in isothermal mode and reproducing experimental trends in the target density profile, which, similarly to the heat flux profile,
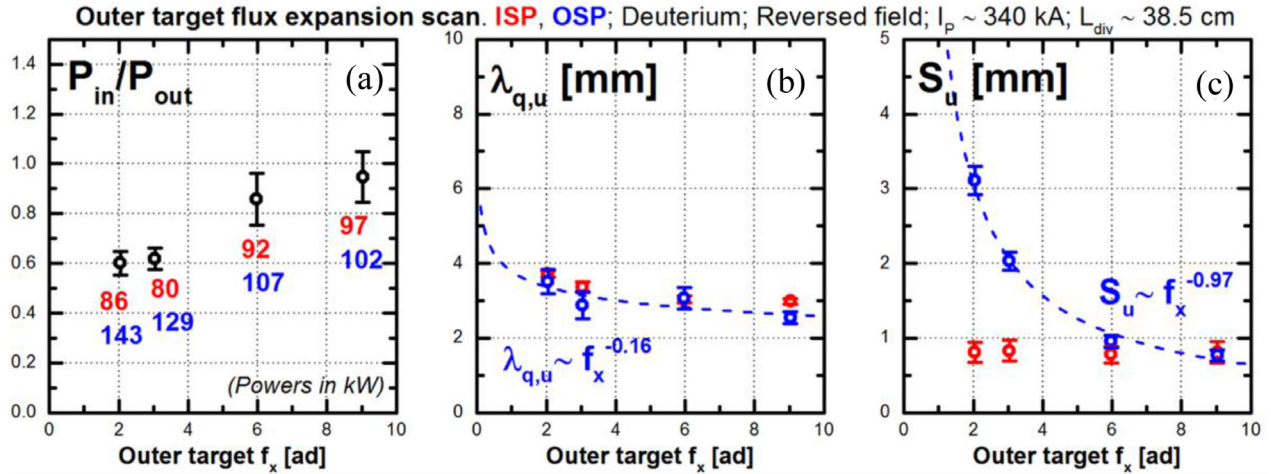
Figure 9. (*a*) Ratio of power fluxes to inner (red) and outer (blue) targets, (*b*) SOL power decay length, (*c*) spreading factor, versus flux expansion. The numbers in (*a*) refer to the individual power exhausted to the inner (red) and outer (blue) targets, in kW. Reproduced courtesy of IAEA. Figure from [83]. Copyright (2018) IAEA.
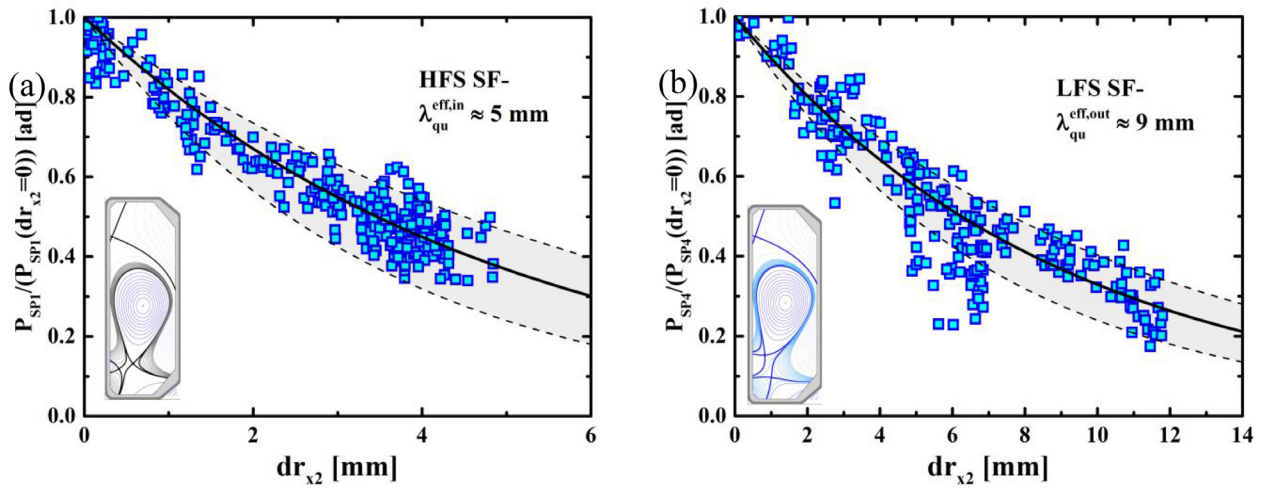
Figure 10. Power flux to outermost secondary strike point as a function of distance between X-points, normalized to its value for zero distance, in a HFS SF- (*a*) and a LFS SF- (*b*). An effective width for the SOL near the secondary X-point is inferred. Reproduced courtesy of IAEA. Figure from [84]. Copyright (2018) IAEA.

shows an asymmetric broadening with leg length. Simulations with the SOLPS-ITER code [82], assuming diffusive, anomalous cross-field transport, were also able to show trends in agreement with the experiments, though further improvement could be achieved by including enhanced transport in the region of unfavorable magnetic curvature.

Increasing the connection length by increasing the poloidal flux expansion has a much weaker effect on λ_q. By contrast, λ_q is found to decrease for increasing plasma current. Both an increase in divertor-leg length and in flux expansion have the effect of reducing the asymmetry in power load at the inner and outer targets—their ratio increasing to nearly unity at the largest values of flux expansion (figure 9) [83]. This variation is attributed to a decrease in the outer conductance, as indicated by EMC3-Eirene simulations. A simple analytical model based on SOL conduction is remarkably successful in reproducing these effects, including the dependence of λ_q on plasma current [79]. The difference in λ_q between the inner

and the outer divertor, as well as a dependence on the magnetic-field direction, are however not captured by this model.

A study of transport and heat loads was conducted on the alternative SF-divertor configuration, using a fast reciprocating probe in addition to infrared thermography [84]. The power sharing between the inner and the outer divertor is modified by the appearance and position of the secondary X-point. A simple analytical model is used to derive a single effective width of the SOL heat-flux profile in the low-poloidal-field region. This width is found to be similar in the SN and HFS SF-configurations, whereas it doubles in the LFS SF-, even though the outer-midplane SOL profiles are similar (figure 10). The increased diffusivity in the latter case cannot be explained by the pressure-driven plasma convection expected near the primary X-point, whereas it is consistent with ballooning interchange turbulence enhanced by the low poloidal field [84]. In the forward ∇B drift direction, the SF- exhibits double-peaked particle- and heat-flux profiles, which previous

simulations were unable to reproduce. The simple conductance model described before also fails for this particular case [79]. The 2D edge transport code UEDGE was used—only on SN discharges thus far—to test the hypothesis that these discrepancies may be due to ExB drifts in addition to turbulent processes. The code was able to reproduce the double peaks whereas a control run with the drifts turned off did not; the variation in density and temperature between the forward- and reversed-field cases is also reproduced successfully, although minor discrepancies persist [85].

The effect of shaping was explored through a scan of the upper triangularity δ_{up} from negative to positive, in deuterium and helium plasmas and in both forward and reversed field [86]. The outer-divertor λ_q was found to be larger in helium (as in AUG) and to increase with δ_{up}. The inner-divertor λ_q, by contrast, is non-monotonic and reaches a maximum at $\delta_{up} = 0$. The direction of the field is immaterial. This dependence on δ_{up} is not captured by standard scalings but is consistent with one scaling containing a dependence on the edge temperature [87], which is found to decrease with δ_{up} [86].

A limited study of heat expulsion by ELMs was conducted, in conjunction with AUG, with the specific aim of determining under which circumstances a second, slower ELM crash follows the first one, increasing the total energy released. The answer is that the second crash is observed only at high density and with intense fueling. The hypothesis that the second ELM crash is related to a threshold in pedestal pressure is disproven by this dataset [88].

5.2.2. Limited plasmas: the narrow SOL feature. It is by now well documented that inside-limited L-mode plasmas frequently exhibit a two-slope SOL parallel-heat-flux profile, which results in an enhanced wall heat load, potentially dangerous to a reactor during the limited ramp-up phase. It was reported earlier that the narrow feature disappears on TCV at low plasma current or high density [89]. A more recent study was specifically conducted using the reciprocating probe on the outboard side. A narrow feature is seen there but is considerably wider than that inferred from thermography measurements on the inboard side. However, the calculated power fraction contained in the feature is found to be equal for the two measurements, indicating that it is indeed the same phenomenon. The width of the feature is determined to scale with the radial correlation length of the turbulence, as is expected on theoretical grounds if it is due to sheared $E \times B$ drifts [90].

Nitrogen impurity seeding also has been demonstrated to eliminate this feature when the radiated power fraction exceeds 60%. The attendant 30% increase in effective charge may well be a tolerable price for the mitigated power flux. In addition, a radiative mantle is seen to persist long after the injection, resulting in enhanced core temperature [91].

5.2.3. Wall heat-flux control. A wide-angle visible and infrared viewing system is planned for ITER to protect the plasma-facing components (PFCs) from excessive power deposition in real time [92]. A model-based controller, which accounts for 3D effects in the PFCs, is being developed for this task. The controller is based on real-time equilibrium reconstruction,
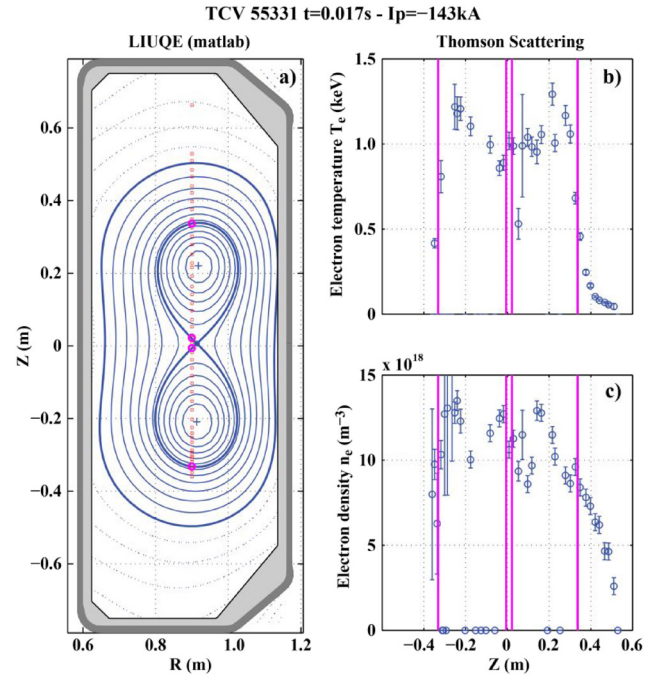
Figure 11. (*a*) Equilibrium reconstruction for a doublet configuration; (*b*) electron-temperature and (*c*) density profiles along the vertical Thomson scattering chord. The vertical lines are the reconstructed lobe extremities. Reproduced with permission from [101].

which is then used to describe the deposited heat flux as a magnetic-flux function with user-specified parameters for the power exhausted into the SOL and the SOL heat-flux width. The heat-flux observer has been validated in limited plasmas in TCV and was found to be in good agreement with the heat flux determined from infrared thermography [93].

5.3. SOL turbulence and transport

SOL turbulence studies focus primarily on the larger, field-aligned intermittent structures known as *filaments* or *blobs*. Considerable data analysis work has gone in particular into investigating the possible relation between filaments (characterized by the TCV reciprocating probe) and the flattened upstream density-profile feature observed in the SOL in many scenarios and termed the *density shoulder*. Density ramps with varying outer-target flux expansion were used to determine that (a) the filament size increases with density but is insensitive to the connection length, (b) the density gradient length increases with density in the near SOL but is unaffected in the far SOL, while both are insensitive to the connection length. It is concluded that flux expansion is not a viable tool to affect the density profile. It is believed that the shoulder formation requires high collisionality, but this appears not to be a sufficient condition in TCV [94].

These studies were extended more recently, in conjunction with AUG, through plasma current scans—both at constant toroidal magnetic field and at constant q_{95}. No clear trend is evinced in the latter case, whereas at constant B_T the shoulder is formed at lower edge density when current is lower, consistent with an underlying dependence on the Greenwald
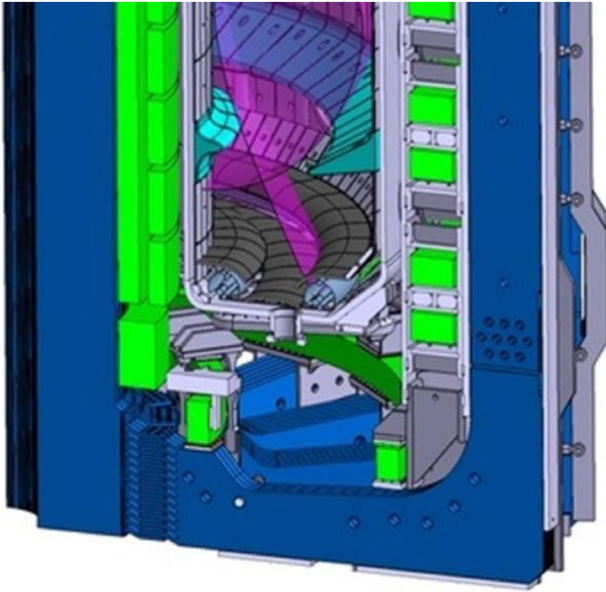
Figure 12. TCV divertor upgrade, showing the baffles (cyan) and the cryo-pumps under consideration (light blue). Reprinted from [103], Copyright (2017), with permission from Elsevier.

fraction. Unlike on AUG [95], no clear correlation is found between the shoulder appearance and either filament size or divertor collisionality. As filaments in both devices originate primarily from resistive ballooning instabilities, the different behavior must be associated with other mechanisms—arising, presumably, from the radically different divertor geometry (closed in AUG, open in TCV) [95].

An extensive reciprocating-probe database was constructed for TCV and mined with novel analysis techniques to study the scalings of the radial velocity of filaments, motivated by analytical theory predictions [96] and with the goal of refining models that are crucial for the understanding of SOL transport. In absolute terms, filament diameters lie typically in the 3–11 mm range and their radial velocities are between 0.5–2 km s^{-1} (outward); however, significant tails exist in the distribution and, in particular, inward velocities are observed for the first time, only in reversed field (ion ∇B drift pointing away from the X-point) and in conditions of high poloidal-velocity shear. The *maximum* velocity is a function of filament size and of divertor collisionality as predicted by theory, but the velocity of most filaments is in fact independent of collisionality owing to their resistive-ballooning character, which explains the insensitivity of velocity to density and connection length [97].

A study of flows and fluctuations in the low-poloidal-field region of a LFS SF-plasma was conducted with a fast framing visible-light camera. As the normalized distance σ between X-points decreases, the flow in the outer SOL is unchanged, whereas it increases in the inner SOL; at the same time, the fluctuations between the X-points become uncorrelated from those above the primary X-point, suggesting the formation of filaments in the low-$B_{\rm p}$ region. In addition, the dominant motion of these filaments turns from poloidal to radial as σ

decreases, consistent with an enhancement of cross-field transport [98].

6. Doublets

Beyond all current 'alternative' scenarios lies a long-dormant topological concept, the doublet [99, 100] (with a figure-of-eight flux-surface featuring an internal X-point), which is believed to afford the benefits of high elongation with increased vertical stability [99] and promises tantalizing new physics associated with its internal X-point. The primary difficulty associated with this configuration is the inherent tendency of the two lobes to collapse into one, owing either to the magnetic attraction between the two current channels or to a thermal instability favoring one lobe over the other. With a uniquely suited coil set, TCV was the natural device on which to revisit this possibility using modern control technology. In preparation for this attempt, extensive work went into tuning the plasma control system to improve and optimize the plasma breakdown and burn-through, which had a non-negligible failure rate. Proper consideration of the large currents circulating in the conducting vessel during this phase was required for this task. With these tools in hand, a double breakdown and ramp-up was attempted, with only partial success in that the top lobe always coalesced rapidly into the lower one. The next step was to apply ECRH power separately to the two lobes, each controlled from its own lobe current observer, in an attempt to equalize the currents. A successful doublet was maintained in this manner for ~30 ms, with a current up to 270 kA and peak electron temperature 1.3 keV in both lobes (figure 11). These initial data suggest the appearance of a transport barrier in the negative-shear mantle just outside the internal separatrix [101]. Power and deposition scans also showed that the scenario was surprisingly robust against coalescence, suggesting that the transport barrier common to both lobes effectively sets the boundary condition for both and results in similar pressure profiles irrespective of the input power apportionment. The reasons for the disruption at ~30 ms are not currently understood, and additional research is planned to be conducted towards achieving steady state.

7. Conclusions and outlook

TCV is documenting the physics basis for ITER and exploring avenues for solving its most pressing concerns, while also casting a wide net in configuration space to identify viable alternatives for DEMO and an eventual fusion reactor. The experimental campaigns of the past two years have brought significant advances on all these fronts.

Looking to the near future, a substantial upgrade program is now in full swing [102]. Additional auxiliary heating sources are being added as discussed in the introduction. Even more momentously, in-vessel baffles will be added to equip TCV with a partially closed divertor for the first time, allowing it to reach reactor-relevant neutral density and

impurity compression [103]. We plan to fabricate baffles of different sizes, to be swapped in relatively short interventions, in order to vary the divertor closure and investigate how this affects plasma performance. The first set to be installed comprises 32 baffles on the HFS and 64 on the LFS [104] (figure 12). Simulations with SOLPS-ITER and EMC3-Eirene were performed to guide the design [103]. For enhanced control of the plasma and of the divertor region, dedicated pumps (e.g. cryo-pumps) are also under consideration in addition to toroidally distributed fuel and impurity injection valves. A phased program of diagnostic additions and upgrades is also in place. The first new diagnostics to be associated with the vessel upgrade will be ~50 new Langmuir probes, baratron gauges, infrared thermography, bolometry, divertor spectroscopy, divertor Thomson scattering, and additional Mirnov coils [102]. Note that most of TCV's versatility in plasma shaping will be preserved with this upgrade, which is in any case modular and reversible. This upgrade has been designed with the express goal of extending the TCV research program well into the ITER era.

Acknowledgments

ORCID iDs

S. Coda ⓘ https://orcid.org/0000-0002-8010-4971
M. Agostini ⓘ https://orcid.org/0000-0002-3823-1002

References

[1] Hofmann F. *et al* 1994 *Plasma Phys. Control. Fusion* **36** B277
[2] Meyer H. *et al* 2017 *Nucl. Fusion* **57** 102014
[3] Goodman T.P. *et al* 2008 *Nucl. Fusion* **48** 054011
[4] Alberti S. *et al* 2017 *EPJ Web Conf.* **157** 03001
[5] Karpushov A.N. *et al* 2017 *Fusion Eng. Des.* **123** 468
[6] Vallar M. *et al* 2019 *Fusion Eng. Des.* accepted (https://doi.org/10.1016/j.fusengdes.2019.01.077)
[7] Hawke J. *et al* 2017 *J. Instrum.* **12** C12005
[8] Rabinski M. *et al* 2017 *J. Instrum.* **12** C10014
[9] Esposito B. *et al* 2017 *Plasma Phys. Control. Fusion* **59** 014044
[10] Linehan B.L. *et al* 2018 *Rev. Sci. Instrum.* **89** 103503
[11] Wijvers W.A.J. *et al* 2017 *J. Instrum.* **12** C12058
[12] Molina Cabrera P. *et al* 2018 *Rev. Sci. Instrum.* **89** 083503
[13] Molina Cabrera P. *et al* 2018 *45th Conf. on Controlled Fusion and Plasma Physics, Europhysics Conf. Abstracts (Prague)* vol 42A P1.1015 (http://ocs.ciemat.es/EPS2018PAP/pdf/P1.1015.pdf)
[14] Meyer H. *et al* 2019 *Nucl. Fusion* **59** 112014
[15] Eidietis N.W. *et al* 2015 *Nucl. Fusion* **55** 063030
[16] Maraschek M. *et al* 2018 *Plasma Phys. Control. Fusion* **60** 014047
[17] Sheikh U. *et al* 2018 *Nucl. Fusion* **58** 106026
[18] Galperti C. *et al* 2017 *IEEE Trans. Nucl. Sci.* **64** 1446
[19] Reich M. *et al* 2015 *Fusion Eng. Des.* **100** 73
[20] Maraschek M. *et al* 2013 *40th Conf. on Controlled Fusion and Plasma Physics, Europhysics Conf. Abstracts (Espoo)* vol 37D P4.127 (http://ocs.ciemat.es/EPS2013PAP/pdf/P4.127.pdf)
[21] Blanken T. *et al* 2019 *Nucl. Fusion* **59** 026017
[22] Pau A. *et al* 2018 *IEEE Trans. Plasma Sci.* **46** 2691
[23] Pau A. *et al* 2017 *Fusion Eng. Des.* **125** 139
[24] Pau A. *et al* 2017 *44th Conf. on Controlled Fusion and Plasma Physics, Europhysics Conf. Abstract (Belfast)* vol 41F P2.134 (http://ocs.ciemat.es/EPS2017PAP/pdf/P2.134.pdf)
[25] Plyusnin V.V. *et al* 2018 *Nucl. Fusion* **58** 016014
[26] Carnevale D. *et al* 2019 *Plasma Phys. Control. Fusion* **61** 014036
[27] Schweinzer J. *et al* 2016 *Nucl. Fusion* **56** 106007
[28] Whyte D.G. *et al* 2010 *Nucl. Fusion* **50** 105005
[29] Piron C. *et al* 2017 *44th Conf. on Controlled Fusion and Plasma Physics, Europhysics Conf. Abstract (Belfast)* vol 41F P1.153 (http://ocs.ciemat.es/EPS2017PAP/pdf/P1.153.pdf)
[30] Piron C. *et al* 2018 Extension of the operating space of high-β_N fully noninductive scenarios on TCV using neutral beam injection *Preprint: 2018 IAEA Fusion Energy Conf. (Gandhinagar, India, 22–27 October 2018)* EX/P1-30
[31] Vallar M. *et al* 2018 *45th Conf. on Controlled Fusion and Plasma Physics, Europhysics Conf. Abstract (Prague)* vol 42A P2.1068 (http://ocs.ciemat.es/EPS2018PAP/pdf/P2.1068.pdf)
[32] Kong M. *et al* 2017 *44th Conf. on Controlled Fusion and Plasma Physics, Europhysics Conf. Abstract (Belfast)* vol 41F P4.152 (http://ocs.ciemat.es/EPS2017PAP/pdf/P4.152.pdf)
[33] Kong M. *et al* 2019 *Nucl. Fusion* **59** 076035
[34] Rispoli N. *et al* 2019 *Fusion Eng. Des.* accepted (https://doi.org/10.1016/j.fusengdes.2019.01.051)
[35] Villone F. *et al* 2018 *45th Conf. on Controlled Fusion and Plasma Physics, Europhysics Conf. Abstract (Prague)* vol 42A P5.1054 (http://ocs.ciemat.es/EPS2018PAP/pdf/P5.1054.pdf)
[36] Maljaars E. *et al* 2017 *Nucl. Fusion* **57** 126063
[37] Mavkov B. *et al* 2018 *Nucl. Fusion* **58** 056011
[38] Vu N.M.T. *et al* 2017 *Fusion Eng. Des.* **123** 624
[39] Marco A. *et al* 2018 *World Automation Congress (Stevenson, WA, USA)* (IEEE) p 253 (https://ieeexplore.ieee.org/document/8430383)
[40] Anand H. *et al* 2017 *Nucl. Fusion* **57** 126026
[41] Pesamosca F. *et al* 2018 *45th Conf. on Controlled Fusion and Plasma Physics, Europhysics Conf. Abstract (Prague)* vol 42A P1.1079 (http://ocs.ciemat.es/EPS2018PAP/pdf/P1.1079.pdf)
[42] Felici F. *et al* 2018 *Nucl. Fusion* **58** 096006
[43] Teplukhina A.A. *et al* 2017 *Plasma Phys. Control. Fusion* **59** 124004
[44] Carpanese F. *et al* 2018 *45th Conf. on Controlled Fusion and Plasma Physics, Europhysics Conf. Abstract (Prague)* vol 42A P2.1050 (http://ocs.ciemat.es/EPS2018PAP/pdf/P2.1050.pdf)
[45] Coelho R. *et al* 2017 *44th Conf. on Controlled Fusion and Plasma Physics, Europhysics Conf. Abstract (Belfast)* vol 41F P2.137 (http://ocs.ciemat.es/EPS2017PAP/pdf/P2.137.pdf)
[46] Poli E. *et al* 2018 *Comput. Phys. Commun.* **225** 36
[47] Weiland M. *et al* 2018 *Nucl. Fusion* **58** 082032
[48] Vu N.M.T. *et al* 2019 *Nucl. Fusion* submitted
[49] Shirai H. *et al* 2017 *Nucl. Fusion* **57** 102002
[50] Douai D. *et al* 2018 *Nucl. Fusion* **58** 026018

[51] Ricci D. *et al* 2018 *45th Conf. on Controlled Fusion and Plasma Physics, Europhysics Conf. Abstract (Prague)* vol 42A P4.1074 (http://ocs.ciemat.es/EPS2018PAP/pdf/P4.1074.pdf)

[52] Sheikh U. *et al* 2019 *Plasma Phys. Control. Fusion* **61** 014002

[53] Dunne M. *et al* 2017 *Plasma Phys. Control. Fusion* **59** 014017

[54] Snyder P. *et al* 2009 *Phys. Plasmas* **16** 056118

[55] Frassinetti L. *et al* 2019 *Nucl. Fusion* **59** 076038

[56] Pochelon A. *et al* 2012 *Plasma Fusion Res.* **7** 2502148

[57] Merle A. *et al* 2017 *Plasma Phys. Control. Fusion* **59** 104001

[58] Stober J. *et al* 2001 *Nucl. Fusion* **41** 1123

[59] Labit B. *et al* 2019 *Nucl. Fusion* **59** 086020

[60] Cruz N. *et al* 2018 *Fusion Eng. Des.* **129** 247

[61] Mariani A. *et al* 2018 *Phys. Plasmas* **25** 012313

[62] Ball J. *et al* 2018 *Nucl. Fusion* **58** 026003

[63] Marini C. 2017 *PhD Thesis* EPFL

[64] Geiger B. *et al* 2017 *Plasma Phys. Control. Fusion* **59** 115002

[65] Camenen Y. *et al* 2007 *Nucl. Fusion* **47** 510

[66] Fontana M. *et al* 2018 *Nucl. Fusion* **58** 024002

[67] Huang Z. *et al* 2019 *Plasma Phys. Control. Fusion* **61** 014021

[68] Merlo G. *et al* 2015 *Plasma Phys. Control. Fusion* **57** 054010

[69] Huang Z. *et al* 2018 *Plasma Phys. Control. Fusion* **60** 034007

[70] Merlo G. *et al* 2018 *Plasma Phys. Control. Fusion* **60** 034003

[71] Chellai O. *et al* 2019 *Plasma Phys. Control. Fusion* **61** 014001

[72] Février O. *et al* 2018 *Rev. Sci. Instrum.* **89** 053502

[73] Maurizio R. *et al* 2017 *44th Conf. on Controlled Fusion and Plasma Physics, Europhysics Conf. Abstract (Belfast)* vol 41F P5.116 (http://ocs.ciemat.es/EPS2017PAP/pdf/P5.116.pdf)

[74] Février O. *et al* 2018 *45th Conf. on Controlled Fusion and Plasma Physics, Europhysics Conf. Abstract (Prague)* vol 42A P2.1040 (http://ocs.ciemat.es/EPS2018PAP/pdf/P2.1040.pdf)

[75] Verhaegh K. *et al* 2017 *Nucl. Mater. Energy* **12** 1112

[76] Fil A. *et al* 2018 *Contrib. Plasma Phys.* **58** 746

[77] Theiler C. *et al* 2018 SOL transport and detachment in alternative divertor configurations in TCV L- and H-mode plasmas *Preprint: 2018 IAEA Fusion Energy Conf. (Gandhinagar, India, 22–27 October 2018)* EX/P1-19

[78] Harrison J. *et al* 2019 *Plasma Phys. Control. Fusion* **61** 065024

[79] Maurizio R. *et al* 2018 *Nucl. Mater. Energy* **19** 372

[80] Eich T. *et al* 2013 *Nucl. Fusion* **53** 093031

[81] Gallo A. *et al* 2018 *Plasma Phys. Control. Fusion* **60** 014007

[82] Wensing M. *et al* 2018 *45th Conf. on Controlled Fusion and Plasma Physics, Europhysics Conf. Abstract (Prague)* vol 42A O4.107 (http://ocs.ciemat.es/EPS2018PAP/pdf/O4.107.pdf)

[83] Maurizio R. *et al* 2018 *Nucl. Fusion* **58** 016052

[84] Maurizio R. *et al* 2019 *Nucl. Fusion* **59** 016014

[85] Christen N. *et al* 2017 *Plasma Phys. Control. Fusion* **59** 105004

[86] Faitsch M. *et al* 2018 *Plasma Phys. Control. Fusion* **60** 045010

[87] Sieglin B. *et al* 2016 *Plasma Phys. Control. Fusion* **58** 055015

[88] Frassinetti L. *et al* 2017 *44th Conf. on Controlled Fusion and Plasma Physics, Europhysics Conf. Abstract (Belfast)* vol 41F P5.135 (http://ocs.ciemat.es/EPS2017PAP/pdf/P5.135.pdf)

[89] Nespoli F. *et al* 2017 *Nucl. Fusion* **57** 126029

[90] Tsui C.K. *et al* 2017 *Phys. Plasmas* **24** 062508

[91] Nespoli F. *et al* 2018 *Phys. Plasmas* **25** 052501

[92] Anand H. *et al* 2018 Implementation of 3D effects of the ITER plasma-facing components in a 2D real-time model-based approach for wall heat flux control on ITER *Preprint: 2018 IAEA Fusion Energy Conf. (Gandhinagar, India, 22–27 October 2018)* EX/P7-24

[93] Anand H. *et al* 2018 *45th Conf. on Controlled Fusion and Plasma Physics, Europhysics Conf. Abstract (Prague)* vol 42A P2.1074 (http://ocs.ciemat.es/EPS2018PAP/pdf/P2.1074.pdf)

[94] Vianello N. *et al* 2017 *Nucl. Fusion* **57** 116014

[95] Vianello N. *et al* 2019 SOL transport and filamentary dynamics in high density tokamak regimes *Preprint: 2018 IAEA Fusion Energy Conf. (Gandhinagar, India, 22–27 October 2018)* EX/P8-13

[96] Myra J.R. *et al* 2006 *Phys. Plasmas* **13** 112502

[97] Tsui C.K. *et al* 2018 *Phys. Plasmas* **25** 072506

[98] Walkden N.R. *et al* 2018 *Plasma Phys. Control. Fusion* **60** 115008

[99] Jensen T.H. *et al* 1975 *Phys. Rev. Lett.* **34** 257

[100] Wesley J. *et al* 1980 *Proc. 8th Int. Conf. on Plasma Physics and Controlled Nuclear Fusion Research (Brussels)* (Vienna: IAEA) vol 1, p 35

[101] Duval B.P. *et al* 2018 Singlet breakdown optimization to a doublet plasma configuration on the TCV tokamak *Preprint: 2018 IAEA Fusion Energy Conf. (Gandhinagar, India, 22–27 October 2018)* EX/P1-6

[102] Fasoli A. for the TCV Team 2019 TCV heating and divertor upgrades *Preprint: 2018 IAEA Fusion Energy Conf. (Gandhinagar, India, 22–27 October 2018)* FIP/P8-6

[103] Reimerdes H. *et al* 2017 *Nucl. Mater. Energy* **12** 1106

[104] Vaccaro D. *et al* 2019 *Fusion Eng. Des.* accepted (https://doi.org/10.1016/j.fusengdes.2019.02.125)